Influence of Ch substitution on structural, electronic, and thermoelectric properties of layered oxychalcogenides (La$_{0.5}$Bi$_{0.5}$O)CuCh (Ch = S, Se, Te): a new insight from first principles

Shibghatullah Muhammady, [iD] Rena Widita and Yudi Darma [iD] *

We study the structural, electronic, and thermoelectric properties of p-type layered oxychalcogenides (La$_{0.5}$Bi$_{0.5}$O)CuCh (Ch = S, Se, Te) from first principles. Ch substitution from S to Te enhances the local-symmetry distortions (LSDs) in CuCh$_4$ and OLa$_2$Bi$_2$ tetrahedra, where the LSD in OLa$_2$Bi$_2$ is more pronounced. The LSD in CuCh$_4$ tetrahedra comes from the possible pseudo-Jahn–Teller effect, indicated by the degeneracy-lifted t$_{2g}$ and e$_g$ states of Cu 3d^{10} orbital. The Ch substitution decreases bandgap from 0.529, 0.256 ($\Gamma \rightarrow 0.4\Delta$), to 0.094 eV (Z $\rightarrow 0.4\Delta$), for Ch = S, Se, Te, respectively, implying the increasing carrier concentration and electrical conductivity. The split-off energy at Z and Γ points are also increased by the substitution. The valence band shows deep O 2p states in the electron-confining [LaBiO$_2$]$^{2+}$ layers, which is essential for thermoelectricity. (La$_{0.5}$Bi$_{0.5}$O)CuTe provides the largest thermoelectric power from the Seebeck coefficient and the carriers concentration, which mainly come from Te 5p$_x$/p$_y$, Cu 3d$_{zx}$, and Cu 3d$_{zy}$ states. The valence band shows the partial hybridization of t$_{2g}$ and Chp states, implied by the presence of nonbonding valence t$_{2g}$ states. This study provides new insights, which predict experimental results and are essential for novel functional device applications.

1. Introduction

Renewable energy sources are globally researched but maximizing their energy efficiency is challenging. Moreover, energy waste as thermal energy cannot be avoided in energy conversion processes. This condition leads to an increase in energy consumption. For the utilization of the energy waste, the thermal energy can be recovered and provide clean energy using the thermoelectric effect, which generates electric power from temperature (T, in K) gradient.[1–5] The thermoelectric effect is measured by the figure of merit (ZT) formulated by

$$ZT = \frac{S^2 \sigma T}{\kappa} \quad \text{(dimensionless)} \quad (1)$$

where S is the Seebeck coefficient (in V K^{-1}), σ is the electrical conductivity (in S m^{-1}), and κ is the thermal conductivity (in W m^{-1} K^{-1}).[1,6] S can be expressed by the Mott formula,[7,8] which is formulated by

$$S = \frac{\pi^2 k_B^2 T}{3q} \left[\frac{1}{D(E)} \frac{dD(E)}{dE} + \frac{1}{\mu(E)} \frac{d\mu(E)}{dE} \right]_{E=E_F} \quad \text{(in V K}^{-1}) \quad (2)$$

Department of Physics, Faculty of Mathematics and Natural Sciences, Institut Teknologi Bandung, Ganesha 10, Bandung, 40132, Indonesia. E-mail: yudi@fi.itb.ac.id

where q is the elementary charge ($q = 1.602 \times 10^{-19}$ C), k_B is the Boltzmann constant ($k_B = 1.381 \times 10^{-23}$ J K^{-1}), and $\mu(E)$ is the mobility (in m^2 V^{-1} s^{-1}). Furthermore, S, σ, and κ are dependent on each other as the functions of the carrier concentration (n, in m^{-3}) and the electronic properties. Notably, κ is contributed by two sources, that are transporting heat of electrons and holes (κ_e), which is a function of σ, and phonons passing through crystal lattices (κ_l). This condition leads to the challenging attempts for finding the optimum values of these parameters for obtaining the high ZT.[1,9]

The superlattice structures are promising in generating the thermoelectric effect. The p-type Bi$_2$Te$_3$/Sb$_2$Te$_3$ superlattice structure shows the high thermoelectric power with ZT up to 2.4 at room temperature (RT), which is the result of the optimum control of electrons and phonons.[10] The similar superlattice structure, accompanied by n-type δ-doped Bi$_2$Te$_{3-x}$Se$_x$ in the superlattice thermoelectric modules, show the high cooling fluxes, which is potentially useful for modern device applications.[11] Furthermore, the hybrid inorganic–organic superlattice is promising for the flexible thin-film thermoelectric material.[12] Moreover, the natural superlattice (SnS)$_{1.2}$(TiS$_2$)$_2$ has its thermoelectric performance improved in the in-plane direction. Moreover, σ along the in-plane is higher than that of the cross-plane directions, showing the anisotropic behavior. On the other hand, the lattice κ of this system is low because of the phonon scattering in the modulating periodic layers.[13]

The layered oxychalcogenides (RO)TmCh (R = La, Ce, Nd, Pr, Bi; Tm = Cu, Ag; and Ch = S, Se, Te) are the p-type semi-conductors. The systems provide potential applications in thermoelectrics and optoelectronics[14] and are considered as the natural superlattice systems consisting of the insulating oxide and conducting chalcogenide layers.[15–17] The systems have (LaO)AgS-type crystal structure with the space group of $P4/nmm$ (no. 129), in which Ag (O) is tetrahedrally surrounded by S (La) atoms.[18,19] For example, the layered oxychalcogenides (LaO)CuCh show the wide bandgap (E_g) of 2.3 to 3.1 eV by substituting Ch from Te to S, providing potential applications in optoelectronics.[20–25] Also, the excitonic emission at RT has been observed.[26] Our previous report has shown that the dielectric constant (ε_0), the optical dichroism, and the plasmonic states of (LaO)CuCh systems can be tuned by the Ch substitution.[27] However, despite possessing the natural superlattice structure, (LaO)CuCh systems exhibit the low σ, indicating that these systems are not suitable for the thermoelectric application.[25]

Regarding the layered oxychalcogenides, (BiO)CuCh (Ch = Se, Te) are more suitable for the thermoelectric application. (BiO)CuSe show ZT of 0.50 at 923 K, while (BiO)CuTe show ZT of 0.42 and 0.66 at 373 and 673 K, respectively.[6,15] From the experimental and first-principles perspectives, our previous report shows that, in spite of having the lower S than that of (BiO)CuSe system, (BiO)CuTe system provides the larger thermoelectric power due to the high σ and the metallic behavior. Intriguingly, Sr^{2+} and Ca^{2+} doping at Bi site and Ba doping modulation can enhance ZT of (BiO)CuSe system.[28–31] The previous report shows that La doping in (BiO)CuSe increases both σ and κ but decreases S as the La doping concentration (x) increases, leading to the maximum ZT of 0.74 at 923 K for $x = 0.08$. The increase of σ is induced by the significant increase of μ.[32] It has also been shown that the increasing x from 0.02 to 0.06 enhances σ and n but reduces μ at high T. It is suggested that the increase of n is induced by the presence of Bi vacancies due to the doping.[33] On the other hand, the other report shows the increment of μ due to the increasing x.[34] However, doping (BiO)CuTe system for tuning the thermoelectric performance is still a few. For example, the enhancement of the thermoelectric power factor of 16% by Bi addition in (BiO)CuTe system at 723 K has previously been reported.[35] Moreover, structural properties and contributions of orbital states toward the thermoelectric properties of doped (BiO)CuCh are still yet to be explored.

In this paper, we investigate structural, electronic, and thermoelectric properties of layered oxychalcogenides $(La_{0.5}Bi_{0.5}O)CuCh$ (Ch = S, Se, Te) systems calculated by first principles. As the small x tunes the thermoelectricity of La-doped (BiO)CuSe,[32,33] we are interested in the possible role of the same portion of La and Bi elements in inducing new structural, electronic, and thermoelectric properties of $(La_{0.5}Bi_{0.5}O)CuCh$. The results are comprehensively discussed to investigate the effect of Ch substitution on the properties, which are compared to that of (LaO)CuCh and (BiO)CuCh systems. The structural properties were fully optimized to obtain their most stable condition, followed by calculations of band structure, total density of states (TDOS), and projected density of states (TDOS). This study reveals the local-symmetry

distortion (LSD) at $CuCh_4$ and OLa_2Bi_2 tetrahedra, as well as the effect of Ch substitution on both electronic and thermoelectric properties.

2. Computational methodology

The structural and electronic properties of $(La_{0.5}Bi_{0.5}O)CuCh$ (Ch = S, Se, Te) systems (space group: $P4/nmm$)[18,19] were calculated using Quantum-ESPRESSO package code.[36,37] Fig. 1 shows the crystal structure model of $(La_{0.5}Bi_{0.5}O)CuCh$ unit cell. In the unit cell, the system consists of $[LaBiO1O2]^{2+}$ and $[Cu1Cu2Ch1Ch2]^{2-}$ layers showing $CuiCh1_2Ch2_2$ ($i = 1, 2$) and $OkLa_2Bi_2$ ($k = 1, 2$) tetrahedra. Ch1 and Ch2 element are also denoted by Chj ($j = 1, 2$). Table 1 summarizes the initial structural parameters based on that of (LaO)CuCh.[38] The use of i, j, and k is due to the structural symmetry distortion with the presence of two different layers, that are La and Bi layers. The term 'distortion' refers to the fact that the top and the bottom sides of $[Cu1Cu2Ch1Ch2]^{2-}$ layers are located between different La and Bi layers, leading to the decrease of the structural symmetry degree. The structural symmetry distortion will be later discussed in Results and discussions.

The calculation employs the plane-wave method within the generalized gradient approximation (GGA), which includes the Perdew–Burke–Ernzerhof (PBE) exchange–correlation functionals.[39] The previous reports have successfully carried out this method for various systems.[40,41] The norm-conserving pseudo-potential methods are used to approach all-electron potentials. For Cui, Chj, and Ok atoms, the Troullier–Martins (TM) method[42–44] are used, while for La and Bi atoms, the Goedecker–Hartwigsen–Hutter–Teter (GHHT) method[45,46] are used. Note that we use the different pseudopotential methods since this technique can minimize deviations between experimental and calculated structural properties. This technique has been used in our previous report in investigating the structural and electronic properties of (LaO)ZnPn (Pn = P, As, Sb) systems.[47] The
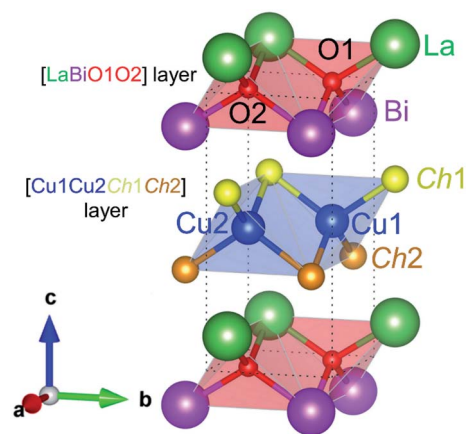

Fig. 1 Crystal structures of $(La_{0.5}Bi_{0.5}O)CuCh$ (Ch = S, Se, Te) systems. The corresponding unit cell consists of [LaBiO1O2] and [Cu₂Ch1Ch2] layers. Notations Ch1 (Ch2) represents Ch between Cu and Bi (La) layers. Blue and red shades denote $CuiCh1_2Ch2_2$ ($i = 1, 2$) and $OkLa_2Bi_2$ ($k = 1, 2$) tetrahedra, respectively.

Table 1 Initial structural parameters of $(La_{0.5}Bi_{0.5}O)CuCh$ (Ch = S, Se, Te) systems

Initial lattice parameter (Å)		$(La_{0.5}Bi_{0.5}O)CuS$	$(La_{0.5}Bi_{0.5}O)CuSe$	$(La_{0.5}Bi_{0.5}O)CuTe$
a		3.9938	4.0670	4.1808
c		8.5215	8.8006	9.3441
Atoms (site symmetry symbol)	Initial atomic positions			
Cui: Cu1 $(x_{Cu}, -y_{Cu}, z_{Cu})$, Cu2 $(-y_{Cu}, x_{Cu}, z_{Cu})$ (2b)	(x_{Cu}, y_{Cu}, z_{Cu})	(1/4, 1/4, 1/2)	(1/4, 1/4, 1/2)	(1/4, 1/4, 1/2)
Ok: O1 $(x_O, -y_O, z_O)$, O2 $(-y_O, x_O, z_O)$ (2a)	(x_O, y_O, z_O)	(1/4, 1/4, 0)	(1/4, 1/4, 0)	(1/4, 1/4, 0)
La (x_{La}, x_{La}, z_{La}), Bi $-(x_{Bi}, x_{Bi}, z_{Bi})$ (2c)	$(x_{La} = x_{Bi}, z_{La} = z_{Bi})$	(1/4, 0.14763)	(1/4, 0.13963)	(1/4, 0.1267)
Chj: Ch1 $(x_{Ch1}, x_{Ch1}, z_{Ch1})$, Ch2 $-(x_{Ch2}, x_{Ch2}, z_{Ch2})$ (2c)	$(x_{Ch1} = x_{Ch2}, z_{Ch1} = z_{Ch2})$	(1/4, 0.6623)	(1/4, 0.6698)	(1/4, 0.6754)

calculation is initiated by the full structural optimization by means of the Broyden–Fletcher–Goldfarb–Shanno (BFGS) method[48–51] with threshold force of ~0.03 eV Å^{-1}. The corresponding command is variable-cell relaxation (vc-relax). Notably, the BFGS method is suitable for large molecular systems.[52] Using this method, the optimized lattice parameters of several systems[53–56] are comparable with that of the corresponding experimental results. Hence, this method is also suitable for small systems. The Broyden mixing method[57] was used for the corresponding self-consistent field (SCF) calculation. The SCF calculation employed threshold and cut-off kinetic energies of ~3.0 and ~1088 eV, respectively, as well as k-point mesh of and 9 × 9 × 4. The SCF calculation was followed by the band structure calculation. A k-point path of Γ–X–R–Z–Γ–M–A–Z is used in the corresponding Brillouin zone. In the whole paper, visualizations of all crystal structures and calculations of LSD parameters are performed using VESTA.[58] Any term of 'Ch substitution' refers to the Ch substitution from S to Te.

3. Results and discussion

3.1. Structural properties

Table 2 presents the calculated structural parameters of $(La_{0.5}Bi_{0.5}O)CuCh$ (Ch = S, Se, Te) systems compared with that of the previous experimental reports of (LaO)CuCh and (BiO)CuCh systems.[38] The structural parameters include the lattice parameters a and c. We use a general term $\Delta\eta$ to represent Δa and Δc, which is the difference percentage between calculated data (η_{calc}) and experimental results (η_{exp}). This term is expressed as

$$\Delta\eta = [(\eta_{calc}/\eta_{exp}) - 1] \times 100\% \text{ (dimensionless)}. \quad (3)$$

The terms Δa and Δc represent the percentages of the differences between the calculated and experimental a and c, respectively. The calculated a and c are increased by the Ch substitution, as also observed in the experimental for both (LaO)CuCh and (BiO)CuCh systems. This increase is due to the different effective ionic radii of S^{2-}, Se^{2-}, and Te^{2-}, i.e., 1.84, 1.98, and 2.21 Å.[59] Furthermore, the previous experimental results show that both a and c are dependent on La and Bi, summarized in Fig. 2. The calculated results show that a is smaller than that of (LaO)CuCh and larger than that of (BiO)

CuCh systems. On the other hand, the calculated c is larger than that of (LaO)CuCh and larger than that of (BiO)CuCh systems. However, $(La_{0.5}Bi_{0.5}O)CuS$ shows that both a and c are larger than that of the experiments. This result indicates that the co-existence of La and Bi significantly influences both a and c. Moreover, in each $(La_{0.5}Bi_{0.5}O)CuS$ and $(La_{0.5}Bi_{0.5}O)CuTe$ systems, the calculated cell volumes (V_{cell}) are between those of both (LaO)CuCh and (BiO)CuCh (Ch = S, Te) systems, while V_{cell} of $(La_{0.5}Bi_{0.5}O)CuSe$ system is larger than those of both systems.

Each system reveals the structural symmetry distortion, indicated by the fact that the change of atomic positions is no longer only possessed by both z_{La} and z_{Ch}. Instead, all the atoms shift their coordinate components (x, y, z) from the experimental coordinates. The atomic positions of Ok and Cui slightly shift from 2a and 2b sites, respectively, within the $P4/nmm$ space group. In $(La_{0.5}Bi_{0.5}O)CuS$ and $(La_{0.5}Bi_{0.5}O)CuSe$ systems, both x_{Cu} and y_{Cu} are lower than 1/4, while $(La_{0.5}Bi_{0.5}O)CuS$ system shows the opposite result. Moreover, $(La_{0.5}Bi_{0.5}O)CuS$ system shows that z_{Cu} is higher than 1/2, which is in contrast with that of the other systems. Regarding Ok atom, for all the systems, x_O and y_O are slightly higher than 1/4. $(La_{0.5}Bi_{0.5}O)CuS$ shows that z_O is slightly higher (lower) than 1/2, while $(La_{0.5}Bi_{0.5}O)CuTe$ system shows that z_O is slightly lower than 1/2. On the other hand, $(La_{0.5}Bi_{0.5}O)CuSe$ system does not show any z_O shift.

The calculation shows that the atomic positions La, Bi, and Chj shift from their 2c sites. x_{La} and x_{Bi} are lower than 1/4, except x_{Bi} for $(La_{0.5}Bi_{0.5}O)CuS$ and $(La_{0.5}Bi_{0.5}O)CuTe$ systems. On the other hand, x_{Ch1} and x_{Ch2} are higher than 1/4, except x_{Te2}. Furthermore, z_{La} is higher than that of (LaO)CuCh, while z_{Bi} is lower than that of (BiO)CuCh systems. For $(La_{0.5}Bi_{0.5}O)CuS$ and $(La_{0.5}Bi_{0.5}O)CuSe$ systems, z_{Ch1} is lower than that of both (LaO)CuCh and (BiO)CuCh systems, while z_{Ch2} shows the opposite result. These results provide LSD in $CuiCh1_2Ch2_2$ and $OkLa_2Bi_2$ tetrahedra.

The LSD parameters[60,61] are to describe the LSD in $CuiCh1_2Ch2_2$ and $OkLa_2Bi_2$ tetrahedra. First, the mean quadratic elongation (λ_{tet}) is expressed as

$$\lambda_{tet} = 0.25 \sum_{i=1}^{4} (l_i/l_0)^2 \text{ (dimensionless)} \quad (4)$$

where l_0 is A–X bond length for an ideal AX_4 tetrahedron with the same volume with that of the distorted tetrahedron and l_i is A–X bond lengths. The bond-angle variance (θ_{tet}^2) as the second parameter is expressed as

Table 2 Calculated structural parameters of $(La_{0.5}Bi_{0.5}O)CuCh$ (Ch = S, Se, Te) systems (Calc) compared with the previous experimental results denoted by Exp_1 and Exp_2 for (LaO)CuCh and (BiO)CuCh,[38] respectively

Parameter		$(La_{0.5}Bi_{0.5}O)CuS$			$(La_{0.5}Bi_{0.5}O)CuSe$			$(La_{0.5}Bi_{0.5}O)CuTe$		
		Calc	Exp_1	Exp_2	Calc	Exp_1	Exp_2	Calc	Exp_1	Exp_2
a (Å)		3.9699	3.9938(2)	3.8691(1)	4.0413	4.0670(1)	3.9287(1)	4.1442	4.1808(2)	4.0411(2)
c (Å)		8.5791	8.5215(4)	8.5602(4)	8.9197	8.8006(8)	8.9291(2)	9.4662	9.3441(8)	9.5237(5)
Δa (%)		—	−0.5981	2.6056	—	−0.6329	2.8651	—	−0.8746	2.5522
Δc (%)		—	0.6759	0.2207	—	1.3532	−0.1054	—	1.3072	−0.6033
V_{cell} (Å^3)		135.2083	135.9217	128.1456	145.6745	145.5662	137.8178	162.5799	163.3264	155.5267
Cu1 (x_{Cu}, $-y_{Cu}$, z_{Cu})	x_{Cu}	0.2477	1/4		0.2481	1/4		0.2502	1/4	
Cu2 ($-y_{Cu}$, x_{Cu}, z_{Cu})	y_{Cu}	0.2481	1/4		0.2480	1/4		0.2501	1/4	
	z_{Cu}	0.5016	1/2		0.4987	1/2		0.4988	1/2	
O1 (x_O, $-y_O$, z_O)	x_O	0.2500	1/4		0.2500	1/4		0.2502	1/4	
O2 ($-y_O$, x_O, z_O)	y_O	0.2502	1/4		0.2503	1/4		0.2503	1/4	
	z_O	−0.0014	0		0.0000	0		0.0004	0	
La (x_{La}, x_{La}, z_{La})	x_{La}	0.2497	1/4	—	0.2496	1/4	—	0.2499	1/4	—
	z_{La}	0.1566	0.14763(7)	—	0.1458	0.13963(6)	—	0.1280	0.1267(1)	—
Bi $-(x_{Bi}$, x_{Bi}, $z_{Bi})$	x_{Bi}	0.2501	—	1/4	0.2497	—	1/4	0.2501	—	1/4
	z_{Bi}	0.1415	—	0.14829(5)	0.1347	—	0.14020(4)	0.1264	—	0.12733(9)
Ch1 (x_{Ch1}, x_{Ch1}, z_{Ch1})	x_{Ch1}	0.2512	1/4	1/4	0.2510	1/4	1/4	0.2500	1/4	1/4
	z_{Ch1}	0.6567	0.6623(1)	0.6710(2)	0.6684	0.6698(1)	0.6758(1)	0.6771	0.6754(1)	0.6810(1)
Ch2 $-(x_{Ch2}$, x_{Ch2}, $z_{Ch2})$	x_{Ch2}	0.2505	1/4	1/4	0.2507	1/4	1/4	0.2499	1/4	1/4
	z_{Ch2}	0.6722	0.6623(1)	0.6710(2)	0.6768	0.6698(1)	0.6758(1)	0.6772	0.6754(1)	0.6810(1)

$$\theta_{tet}{}^2 = 0.2 \sum_{i=1}^{6} (\theta_i - 109.4712°)^2 \quad (\text{in } °^2) \qquad (5)$$

where θ_i is the X–A–X bond angles.[60] The value of 109.4712° is the bond angle in the ideal tetrahedron.[62]

Table 3 summarizes the average bond length (l_{av}) and the LSD parameters of $(La_{0.5}Bi_{0.5}O)CuCh$ (Ch = S, Se, Te) systems. For all the systems, the Ch substitution increases l_{av}, λ_{tet}, and $\theta_{tet}{}^2$ for both calculated and experimental results.[38] The calculated l_{av} of both $CuiCh1_2Ch2_2$ and $OkLa_2Bi_2$ tetrahedra are higher than that of both (LaO)CuCh and (BiO)CuCh systems, except l_{av} of $OkLa_2Bi_2$ tetrahedra in $(La_{0.5}Bi_{0.5}O)CuTe$ system, which is lower than that of (LaO)CuCh system. Furthermore, both λ_{tet} and $\theta_{tet}{}^2$ of $CuiCh1_2Ch2_2$ tetrahedra are higher than that of (LaO)CuCh but lower than that of (BiO)CuChsystems. In contrast, both λ_{tet} and $\theta_{tet}{}^2$ of $OkLa_2Bi_2$ tetrahedra are lower than that of (LaO)CuCh but higher than that of (BiO)CuCh systems. This result shows the co-existence of La and Bi ions significantly influences the local-symmetry distortion, compared to those of both (LaO)CuCh and (BiO)CuCh systems. For comparing the LSD among the systems, we summarize the LSD parameters from the calculation in Fig. 3. We find that l_{av} of $CuiCh1_2Ch2_2$ tetrahedra are higher than that of $OkLa_2Bi_2$ tetrahedra. Intriguingly, the increases of l_{av} of both $CuiCh1_2$-$Ch2_2$ and $OkLa_2Bi_2$ tetrahedra are almost linear with respect to the Ch substitution, where $CuiCh1_2Ch2_2$ tetrahedra show the larger l_{av} gradient. On the other hand, λ_{tet} and $\theta_{tet}{}^2$ of $OkLa_2Bi_2$ are higher than that of $CuiCh1_2Ch2_2$ tetrahedra. Concerning the Ch substitution, λ_{tet} and $\theta_{tet}{}^2$ increments of $OkLa_2Bi_2$ are also higher than that of $CuiCh1_2Ch2_2$ tetrahedra. This result indicates that the LSD of $OkLa_2Bi_2$ is more sensitive to the Ch substitution than that of $CuiCh1_2Ch2_2$ tetrahedra. Notably, the

LSD of both tetrahedra is induced by the aspiration of the insulating and conducting layers to fit each other on the interface between them. Furthermore, the LSD of $CuiCh1_2Ch2_2$ tetrahedra cannot be provoked by the Jahn–Teller (JT) effect which the fully-occupied Cu 3d orbital cannot possess. We suggest that this LSD is induced by the pseudo-JT effect (PJTE)[63] in $CuiCh1_2Ch2_2$ tetrahedra, which will be discussed later.

3.2. Band structures

The left panels of Fig. 4 present the band structures of $(La_{0.5}Bi_{0.5}O)CuCh$ (Ch = S, Se, Te) systems (range: $-2.8 \leq (E - E_F) \leq 2.8$ eV), zoomed in the right panels (range: $-1.0 \leq (E - E_F) \leq 1.0$ eV). E_F is the Fermi energy level. We find that all the systems are semiconductors, indicated by the presence of E_g. The Ch substitution decreases E_g. The band structures pattern is also modified by the Ch substitution. Fig. 4(d) and (e) show
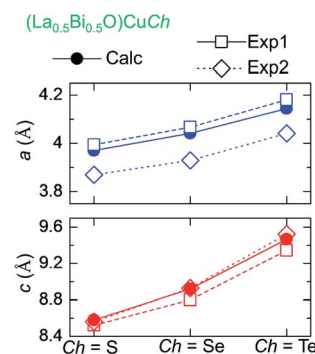

Fig. 2 Trend of lattice parameters of for $(La_{0.5}Bi_{0.5}O)CuCh$ (Ch = S, Se, Te) systems different Ch from calculation (Calc) and experiments of (LaO)CuCh (Exp1) and (BiO)CuCh (Exp2).

Table 3 Average bond length (l_{av}) and local-symmetry distortion parameters (mean quadratic elongation (λ_{tet}), bond-angle variance (θ_{tet}^2)) of CuiCh1$_2$Ch2$_2$ and OkLa$_2$Bi$_2$ tetrahedra in (La$_{0.5}$Bi$_{0.5}$O)CuCh (Ch = S, Se, Te) systems (Calc) compared with the previous experimental results denoted by Exp$_1$ and Exp$_2$ for (LaO)CuCh and (BiO)CuCh,[38] respectively

Tetrahedra	l_{av} (Å)			λ_{tet}			θ_{tet}^2 (°²)		
	Calc	Exp1	Exp2	Calc	Exp1	Exp2	Calc	Exp1	Exp2
(La$_{0.5}$Bi$_{0.5}$O)CuS									
CuiS1$_2$S2$_2$	2.4362	2.4291	2.4259	1.0011	1.0002	1.0021	4.0014	0.7452	8.2968
OkLa$_2$Bi$_2$	2.3619	2.3601	2.3138	1.0049	1.0058	1.0024	18.9186	21.9534	9.4120
(La$_{0.5}$Bi$_{0.5}$O)CuSe									
CuiSe1$_2$Se2$_2$	2.5403	2.5235	2.5145	1.0026	1.0007	1.0068	10.4807	2.6446	27.7188
OkLa$_2$Bi$_2$	2.3770	2.3760	2.3293	1.0081	1.0106	1.0047	30.6467	39.6827	17.9075
(La$_{0.5}$Bi$_{0.5}$O)CuTe									
CuiTe1$_2$Te2$_2$	2.6656	2.6563	2.6560	1.0084	1.0049	1.0164	33.9264	19.5995	67.0207
OkLa$_2$Bi$_2$	2.3967	2.4024	2.3565	1.0164	1.0209	1.0116	60.4193	76.1717	43.0506

that (La$_{0.5}$Bi$_{0.5}$O)CuS and (La$_{0.5}$Bi$_{0.5}$O)CuSe systems have the indirect E_g of 0.529 and 0.256 eV ($\Gamma \rightarrow 0.4\Delta$), respectively. The term 0.4Δ denotes the path connecting 0.4Γ to Z points. These E_g are lower than that of both (LaO)CuCh (1.67 and 1.44 eV for Ch = S and Se, respectively)[27] and (BiO)CuCh systems (0.68 and 0.40 eV for Ch = S and Se, respectively)[64] within the GGA. Furthermore, (La$_{0.5}$Bi$_{0.5}$O)CuTe system exhibits the indirect E_g of 0.094 eV (Z $\rightarrow 0.4\Delta$), which is lower than that of (LaO)CuTe system[27] and shows the different behaviors with that of the metallic (BiO)CuTe system.[64] However, this E_g is close to that of (LaO)CuTe system by including the on-site Coulomb repulsion (U) and spin–orbit coupling (SOC) corrections.[65] We suggest that the decrease E_g corresponds to the increase of the lattice parameters as Ch is substituted from S to Te. The increase of the lattice parameters enlengthens the interatomic distances, leaving binding forces valence electrons and the corresponding parent ions reduced. Thus, the valence electrons are easier to move freely and induce the increase of n and σ. This suggestion assumes that E_g is roughly inversely proportional to n.[66] Hence, the decrease of E_g may indirectly be correlated with the ionic radii of Ch^{2-} ions.

Experimental E_g of all the systems might be higher than that of the present work because of the limitation of the GGA, usually underestimating E_g in the exact Kohn–Sham band structures.[67] Furthermore, including U in the calculation might also provide a closer E_g to that of the possible experimental result. However, U is not suitable to be included in a closed-shell system, where its valence orbitals are in the full occupation or empty.[68] Here, (La$_{0.5}$Bi$_{0.5}$O)CuCh systems are closed-shell systems. The ionic electronic configurations in (La$_{0.5}$Bi$_{0.5}$O)CuCh systems are La^{3+}: [Xe], Bi^{3+}: [Xe] 4f^{14}5d^{10}6s^2, O^{2-}: [He] 2s^{2}2p^6, Cu$^+$: [Ar] 3d^{10}, S^{2-}: [Ne] 3s^{2}3p^6, Se^{2-}: [Ar] 3d^{10}4s^{2}4p^6, and Te^{2-}: [Kr] 4d^{10}5s^{2}5p^6.[69] Also, the exchange–correlation term in Cu 3d orbital cannot be fully described by U.[65,70] The use of hybrid-functional[71–75] or GW approximations[76] might induce the wider E_g than that of the GGA. However, both of them usually overestimate E_g of semiconductors.[77–79] Furthermore, the Hartree–Fock (HF) exchange in the hybrid-

functional approximations can lead to the d-element exchange splitting overestimation.[73,80] These explanation encourages us to keep the GGA method without U correction, thus, indicates that the calculated properties are sufficient to predict experimental electronic properties.

The valence band (VB) structures of (La$_{0.5}$Bi$_{0.5}$O)CuCh (Ch = S, Se, Te) show the tuning of heavy hole (HH), light hole (LH), and split-off hole (SOH) states due to the Ch substitution. We are interested in the k-path of R–Z–Γ–M to observe this tuning since this path is near the E_g transition. Along R–Z path, HH and LH states are separated, followed by SOH. The energy separation between HH and LH states is increased by the Ch substitution, while the energy level of SOH state is pushed down. The
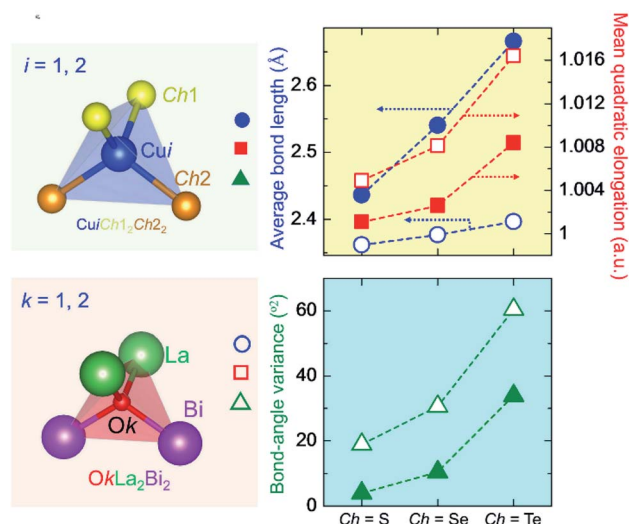

Fig. 3 CuiCh1$_2$Ch2$_2$ (i = 1, 2) (top left panel) and OkLa$_2$Bi$_2$ (k = 1, 2) tetrahedra (bottom left panel) in (La$_{0.5}$Bi$_{0.5}$O)CuCh (Ch = S, Se, Te) systems. The right panels present average bond length and local-symmetry distortion parameters (mean quadratic elongation and bond-angle variance) of both tetrahedra. Filled and unfilled shapes (circle, square, and triangle) denote those of CuiCh1$_2$Ch2$_2$ and OkLa$_2$Bi$_2$ tetrahedra, respectively.
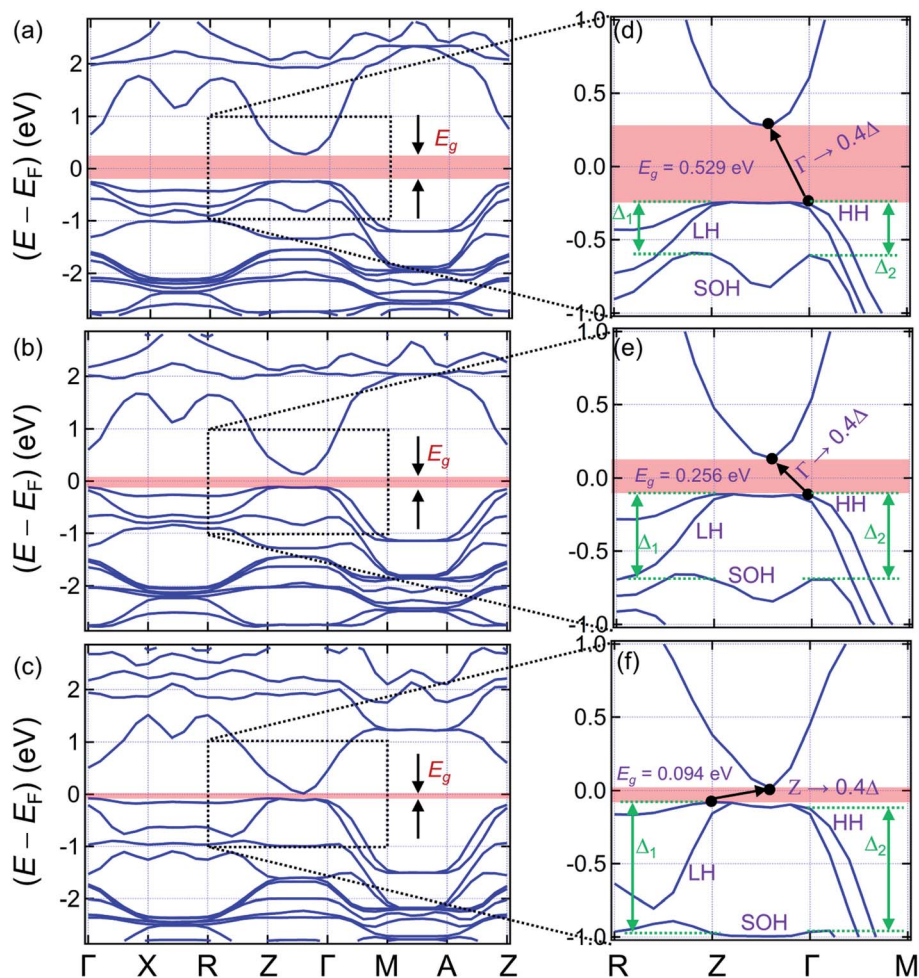
Fig. 4 Band structures of (a) (La$_{0.5}$Bi$_{0.5}$O)CuS, (b) (La$_{0.5}$Bi$_{0.5}$O)CuSe, and (c) (La$_{0.5}$Bi$_{0.5}$O)CuTe systems. (d–f) The right panels show zoomed band structures in the range of $-1.0 < E_F < 1.0$ eV.

increasing separation between HH and LH states is shown by the decrease and increase of steepness of HH and LH states, respectively. Along Z–Γ path, the HH and LH coincide from 0.8Δ to 0.2Δ points. The SOH state shows a valley in the middle of this path, as its energy level is also pushed down by the Ch substitution. Along Γ–M path, the HH and LH states are separated with the lower separation that that of R–Z path. However, this separation is not sensitive to the Ch substitution. On the other hand, the energy level of the SOH state is also sensitively pushed down. We are interested in the shifts of HH, LH, and SOH states at Z and Γ points. By substituting Ch from S to Se, HH, LH, and SOH states show shifts of 137, 122, and −99 meV, respectively, at Z point. At Γ points, HH, LH, and SOH states show shifts of 131, 124, and −88 meV, respectively. By substituting Ch from Se to Te, HH, LH, and SOH states show shifts of 33, −12, and −279 meV, respectively, at Z point. At Γ points, HH, LH, and SOH states show shifts of 0, 3, and −272 meV, respectively. It is indicated that the energy levels of HH and LH states are more sensitive to the Ch substitution from S to Se than that of the SOH state. On the other hand, the energy level of SOH is sensitive to the Ch substitution from Se to Te,

while the energy levels of HH and LH are in contrast. This result leads to a shift of split-off energy (Δ_l) ($l = 1, 2$) of each system, defined as the energy separation between the HH and SOH states. Table 4 presents the split-off energy (Δ_l, $l = 1, 2$) of the systems. The term Δ_1 and Δ_2 are located at Z and Γ points, respectively. The difference between Δ_1 and Δ_2 are defined as δ_{12}. For all the systems, we find the result of $\Delta_1 > \Delta_2$, leading to the positive δ_{12}. Interestingly, the Ch substitution increases both Δ_l and δ_{12}. This result shows the significant role of the Ch substitution in tuning the band structures.

Table 4 Calculated split-off energy (Δ_l) ($l = 1, 2$) of (La$_{0.5}$Bi$_{0.5}$O)CuCh (Ch = S, Se, Te) systems

System	Split-off energy (Δ_l) (in meV)		
	Δ_1 (Z point)	Δ_2 (Γ point)	$\delta_{12} = \Delta_1 - \Delta_2$
(La$_{0.5}$Bi$_{0.5}$O)CuS	350	349	1
(La$_{0.5}$Bi$_{0.5}$O)CuSe	586	569	17
(La$_{0.5}$Bi$_{0.5}$O)CuTe	897	841	56

3.3. Density of states

Fig. 5 presents the TDOS of $(La_{0.5}Bi_{0.5}O)CuCh$ (Ch = S, Se, Te) systems (range: $-8.5 \leq (E - E_F) \leq 5.0$ eV). The TDOS shows the decrease of VB width due to the Ch substitution. We find the VB widths of 6.17, 6.00, and 5.98 eV in $(La_{0.5}Bi_{0.5}O)CuS$, $(La_{0.5}Bi_{0.5}O)CuSe$, and $(La_{0.5}Bi_{0.5}O)CuTe$ systems, respectively. Hence, the Ch substitution slightly enhances the energy localization of VB. The VB can be divided into four levels, *i.e.*, lower bonding, upper bonding, nonbonding, and antibonding levels, as summarized in Table 5. Theoretically, a VB consists of bonding, nonbonding, and antibonding levels. In this work, the four divisions are only to differ between the two peaks of bonding levels. The Ch substitution decreases the lower bonding level and nonbonding level widths but increases the antibonding level width. On the other hand, regarding the upper bonding level, $(La_{0.5}Bi_{0.5}O)CuS$ and $(La_{0.5}Bi_{0.5}O)CuSe$ systems show the lowest and highest level widths, respectively. Furthermore, the Ch substitution decreases the conduction band (CB) width. We find the CB widths of 4.60, 4.34, and 3.91 eV in $(La_{0.5}Bi_{0.5}O)CuS$, $(La_{0.5}Bi_{0.5}O)CuSe$, and $(La_{0.5}Bi_{0.5}O)CuTe$ systems, respectively, indicating the enhancement of energy localization of CB.

Fig. 5 also presents the PDOS of O 2p and Bi 6p states $(La_{0.5}Bi_{0.5}O)CuCh$ (Ch = S, Se, Te) systems. O 2p states of O1 and O2 have the same DOS shape, thus, O 2p states are mentioned without assigning k. We calculate DOS centroids ($E_{centroid}$) for analyzing the PDOS using the expression[81–83]

$$E_{centroid} = \frac{\int_{E_{min}}^{E_{max}} ED(E)dE}{\int_{E_{min}}^{E_{max}} D(E)dE} \approx \frac{\sum_{E_{min}}^{E_{max}} ED(E)\Delta E}{\sum_{E_{min}}^{E_{max}} D(E)\Delta E} \quad \text{(in eV)} \quad (6)$$

where $D(E)$ is the DOS as the function of energy (E). $(La_{0.5}Bi_{0.5}O)CuS$, $(La_{0.5}Bi_{0.5}O)CuSe$, and $(La_{0.5}Bi_{0.5}O)CuTe$ systems show the
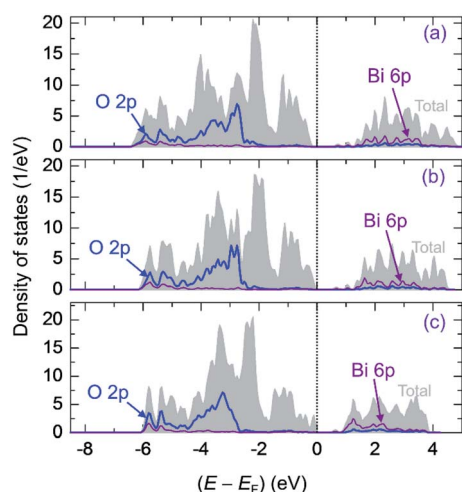
DOS centroids of deep O 2p states of -3.76, -3.73, and -3.95 eV, respectively, as well as the upper limits of high O 2p peaks at -2.54, -2.61, and -2.73 eV, respectively. The upper limits are between that of $(LaO)CuCh$[27] and $(BiO)CuCh$ systems,[64] implying that the co-existence of La and Bi influences the energy level depth of O 2p states. Notably, O 2p states are fully occupied, while La 5d, La 6s, and Bi 6p states are empty in the ionic bonding scheme. However, we find the low-DOS Bi 6p states are shown in the VB, indicating the strong hybridization of O 2p and Bi 6p states. Moreover, the empty La 5d and La 6s are indicated by the absence of both states near E_F. The deep energy level of O 2p states indicates the insulating behavior of $[LaBiO1O2]$ layers, in which the electrons are stable and difficult to be excited to CB. These insulating layers lead to two-dimensional electron confinement in the conducting $[Cu_2\text{-}Ch1Ch2]$ layers. This confinement elucidates that $(La_{0.5}Bi_{0.5}O)CuCh$ can be inferred as natural superlattice systems, which may provide the thermoelectricity applications.[15,16]

Regarding the thermoelectricity, from eqn (2), we predict S using the term $-(dD(E)/dE)$ calculated at $E \sim E_F$. In the present work, the term $-(dD(E)/dE)$ corresponds to hole as carriers for $E < E_F$. The minus $(-)$ sign is used since E below E_F is converted to binding energy, which is represented with the plus sign, as previously shown in the photoemission spectra.[64] Furthermore, we also calculate $n(E)$ expressed as

$$n(E) = D(E)f(E) \text{ (a.u.)} \quad (7)$$

where $f(E)$ is the Fermi–Dirac distribution function.[84] At the ground-state limit, we have $f(E) = 1$ for $E < E_F$. Fig. 6 presents $|dD(E)/dE|$ and $n(E)$ of states $(La_{0.5}Bi_{0.5}O)CuCh$ (Ch = S, Se, Te) systems in a short energy range (range: $-0.2 \leq (E - E_F) \leq 0$ eV). Near E_F, we find $-(dD(E)/dE)$ of 0.21, 17.96, 27.60 eV^{-2} in $(La_{0.5}Bi_{0.5}O)CuS$, $(La_{0.5}Bi_{0.5}O)CuSe$, and $(La_{0.5}Bi_{0.5}O)CuTe$ systems, respectively. We suggest that the higher S of $(La_{0.5}Bi_{0.5}O)CuTe$ than that of $(La_{0.5}Bi_{0.5}O)CuSe$ might provide the higher thermoelectric power. This result is in contrast to that of our previous report that S of $(BiO)CuTe$ is lower than that of $(BiO)CuSe$ systems.[64] However, the larger ZT of $(BiO)CuTe$ provides the higher thermoelectric power due to the metallic behavior, the higher σ, and the lower thermal conductivity (κ) than those of $(BiO)CuSe$ system.[6,15,64] From Fig. 6(b), we show that the Ch substitution enhances $n(E)$ of holes as the carriers, which may lead to the increasing $\sigma(E)$. The term σ is correlated with $n(E)$ and $\mu(E)$ with the expression $\sigma(E) = n(E)\mu(E)q$. We have also proven that the decrease of E_g due to the Ch substitution is proportionally related to the increase of n.[66] The term κ will be presented elsewhere in a future publication. Notably, experimental investigations are opened for clarifying our results.

Fig. 7 presents PDOS of Cui 4s, sub-Chj np (p_x, p_y, p_z), and sub-Cui 3d states in $(La_{0.5}Bi_{0.5}O)CuCh$ (Ch = S, Se, Te) systems. This figure shows the details of orbital contributions to the lower bonding, upper bonding, nonbonding, and antibonding levels in the VB. Notably, the degeneracy-lifted Chj np and Cui 3d orbitals may be induced by the PJTE[63] in the fully-occupied Cui 3d orbital, related to the LSD in $CuiCh1_2Ch2_2$ tetrahedra. Notably, the tetrahedral-type crystal would allow the splitting of

Fig. 5 Total density of states (TDOS) of (a) $(La_{0.5}Bi_{0.5}O)CuS$, (b) $(La_{0.5}Bi_{0.5}O)CuSe$, and (c) $(La_{0.5}Bi_{0.5}O)CuTe$ systems. Projected density of states (PDOS) of O 2p (blue) and Bi 6p states (violet) are also presented.

Table 5 Ranges of divisions in valence band structures of $(La_{0.5}Bi_{0.5}O)CuCh$ (Ch = S, Se, Te) systems

| System | Division level (level width) (in eV) | | | |
	Lower bonding	Upper bonding	Nonbonding	Antibonding
$(La_{0.5}Bi_{0.5}O)CuS$	−6.28 to −4.58 (1.70)	−4.58 to −3.16 (1.42)	−3.16 to −1.42 (1.74)	−1.42 to −0.21 (1.21)
$(La_{0.5}Bi_{0.5}O)CuSe$	−6.09 to −4.50 (1.59)	−4.50 to −2.59 (1.91)	−2.59 to −1.35 (1.24)	−1.35 to −0.09 (1.26)
$(La_{0.5}Bi_{0.5}O)CuTe$	−6.00 to −4.45 (1.55)	−4.45 to −2.67 (1.78)	−2.67 to −1.66 (1.01)	−1.66 to −0.01 (1.65)

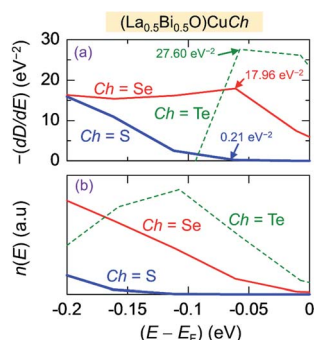**Fig. 6** (a) First derivative of total density of states $-(dD(E)/dE)$ and (b) carriers concentration $n(E)$ of $(La_{0.5}Bi_{0.5}O)CuCh$ (Ch = S, Se, Te) systems as functions of energy (E).

d orbital into 3-fold degenerate Cu 3d-t_{2g} (d_{zx}, d_{zy}, d_{xy}) and 2-fold degenerate Cu 3d-e_g states ($d_{x^2-y^2}$, d_{z^2}). In the present work, each Cu 3d-t_{2g} and Cu 3d-e_g states split into the different energy levels. Even, d_{zx} and d_{zy} states have the different PDOS profile, implying that Cu 3d orbital no longer degenerates. Hence, the PJTE induces the LSD and totally lifts the degeneracy of Cui 3d orbital. We find that Chj np$_x$/p$_y$ states mainly contribute S and $n(E)$, followed by Cu 3d$_{zx}$ and Cu d$_{zy}$ states.

The lower bonding level is contributed by Cui 4s and Chj np states. Based on the theoretical picture, Cu$^+$ 4s orbital should be empty. However, top panels for all the systems show the presence of Cui 4s (PDOS of Cu1 4s = PDOS of Cu2 4s) states in the VB. This result can be induced by the hybridization between Cui

4s and Chj np orbitals. Furthermore, the energy level of this hybridization slightly increases due to the Ch substitution, indicated by the increase of the energy levels of both orbitals. Furthermore, we find that the DOS profiles of Ch1 np and Ch2 np states are different. The different profiles are induced by structural symmetry distortion and the fact that Ch1 and Ch2 are close to the different La and Bi layers, leading to different chemical bonding between Bi–Ch1 and La–Ch2 bonds. In the lower bonding level, the energy levels of Ch2 np states are higher than that of Ch1 np states. We find the two highest peaks of Ch1 np$_z$ and Ch2 np$_z$ states in all the systems, alongside Se2 4p$_x$/p$_y$ peak in $(La_{0.5}Bi_{0.5}O)CuSe$ system. This result indicates that the hybridization between Cui 4s and Chj np along c-axis direction is stronger than that of ab-plane direction.

The upper bonding level is contributed by Cui 3d and Chj np states. In $(La_{0.5}Bi_{0.5}O)CuS$ system, S1 3p$_x$/p$_y$ and S2 3p$_x$/p$_y$ peaks, located at around −4.0 and −4.1 eV, respectively, are the highest peaks among the sub-Chj np states, as presented in Fig. 7(a). At the same energy levels, we find the degeneracy-lifted Cu13d$_{zx}$ and Cu13d$_{zy}$ peaks, as well as the degeneracy-lifted Cu23d$_{zx}$ and Cu23d$_{zy}$ peaks, as shown in Fig. 7(b). This result implies that the upper bonding is more pronounced along ab-plane direction. However, in $(La_{0.5}Bi_{0.5}O)CuSe$ system, Se1 4p$_z$ peak, located at around −3.4, is the highest peak among the sub-Chj np states, followed by Se2 4p$_x$/p$_y$ located at −3.8 eV, as depicted in Fig. 7(c). From Fig. 7(d), at both −3.4 and −3.8 eV, there appear Cui3d$_{z^2}$ and Cu13d$_{zx}$ (Cu23d$_{zy}$) states, respectively, indicating the slightly more pronounced upper bonding along

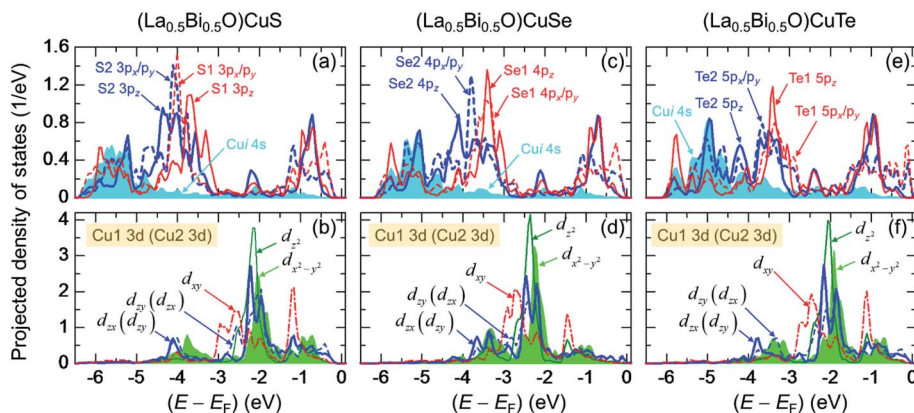**Fig. 7** Projected density of states (PDOS) of Cui 4s, sub-Chj np, and sub-Cui 3d states (i = 1, 2; j = 1, 2) in (a and b) $(La_{0.5}Bi_{0.5}O)CuS$, (c and d) $(La_{0.5}Bi_{0.5}O)CuSe$, and (e and f) $(La_{0.5}Bi_{0.5}O)CuTe$ systems. Notation d$_{zx}$(d$_{zy}$) is used for Cu1(Cu2) since the PDOS of d$_{zx}$ and d$_{zy}$ are the same for Cu1 and Cu2, respectively. This purpose is also used for the notation d$_{zy}$(d$_{zx}$).

c-axis direction. On the other hand, in $(La_{0.5}Bi_{0.5}O)CuTe$ system, Te1 $5p_z$ peak at -3.4 eV is the highest peak among the sub-Ch*j* np states, as shown in Fig. 7(e). Fig. 7(f) shows Cu*i*$3d_{x^2-y^2}$ and Cu1$3d_{zy}$ (Cu2$3d_{zx}$) peaks at the same energy level with that of Te1 $5p_z$ states. This result indicates that Te1 $5p_z$ states experience the strongest hybridization with Cu*i* 3d states compared to the other sub-Te*j* np states. We highlight for all the systems that Cu*i* 3d-t_{2g} states strongly hybridize with Ch*j* np states and also show the larger contribution in the upper bonding level than that of Cu*i* 3d-e_g states.

The nonbonding level is mainly contributed by the localized Cu*i* 3d-e_g states (Cu*i*$3d_{x^2-y^2}$ and Cu*i*$3d_{z^2}$) based on Fig. 7. As the state with the highest peak, Cu*i*$3d_{z^2}$ states are localized at -2.1, -2.4, and -2.1 eV in $(La_{0.5}Bi_{0.5}O)CuS$, $(La_{0.5}Bi_{0.5}O)CuSe$, and $(La_{0.5}Bi_{0.5}O)CuTe$ systems, respectively. From Fig. 7(d), $(La_{0.5}Bi_{0.5}O)CuSe$ system shows the highest peak of Cu*i*$3d_{x^2-y^2}$ states among all the systems. However, the nonbonding level shows the presence of Cu1$3d_{zx}$ (Cu2$3d_{zy}$) and Cu1$3d_{zy}$ (Cu2$3d_{zx}$), indicating that Cu*i* 3d-t_{2g} states partially hybridize with Ch*j* np states. This result is different from the previous suggestion that Cu and Ch ions are bound either along *zx*, *zy*, or *xy* planes.[38] For all the systems, Ch2 np_z also slightly contribute to the nonbonding level, followed by Ch1 np_z states. Additionally, the contribution of Ch1 np_z states is increased by the Ch substitution.

The antibonding level is contributed by Cu*i* 3d and Ch*j* np states. Based on the bottom panels of Fig. 7, all the systems show the highest peaks of Cu*i*$3d_{x^2-y^2}$ states, located at around -1.2, -1.4, and 1.1 eV in $(La_{0.5}Bi_{0.5}O)CuS$, $(La_{0.5}Bi_{0.5}O)CuSe$, and $(La_{0.5}Bi_{0.5}O)CuTe$ systems, respectively. This highest peaks are followed by Cu*i*$3d_{z^2}$ peaks located at the close energy levels to those of Cu*i*$3d_{x^2-y^2}$ states. Regarding Ch*j*, all the systems show the highest peaks of Ch1 np_z and Ch2 np_z states, located at around -0.9 eV based on the top panels of Fig. 7. In $(La_{0.5}Bi_{0.5}O)$CuS system, we find two high peaks of S1 $3p_x/p_y$ and S2 $3p_x/p_y$ states, which are located at -0.4 and -1.2 eV, respectively. In $(La_{0.5}Bi_{0.5}O)CuSe$ and $(La_{0.5}Bi_{0.5}O)CuTe$ systems, the highest Se1 $4p_x/p_y$ (Te1 $5p_x/p_y$) and Se2 $4p_x/p_y$ (Te2 $5p_x/p_y$) peaks are located at -0.3 (-0.1) and -1.1 (-1.2) eV, respectively. This result indicates that the antibonding is more pronounced along *ab*-plane direction. We also highlight for all the systems that Cu*i* 3d-t_{2g} states strongly hybridize with Ch*j* np states and also show the larger contribution in the antibonding level than that of Cu*i* 3d-e_g states.

4. Conclusions

The structural and electronic properties of the layered oxychalcogenides $(La_{0.5}Bi_{0.5}O)$CuCh (Ch = S, Se, Te) have been investigated based on the first principles. From the structural properties, the LSDs in Cu*i*$Ch1_2Ch2_2$ and O*k*La_2Bi_2 tetrahedra are increased by the Ch substitution, in which the LSD in O*k*La_2Bi_2 is stronger than that of $CuCh_4$ tetrahedra. The possible PJTE in the fully-occupied Cu*i* 3d orbital is suggested to be responsible for inducing the LSD in Cu*i*$Ch1_2Ch2_2$ tetrahedra and to lift the degeneracy level of t_{2g} and e_g states. From the electronic properties, all the systems are semiconductors.

$(La_{0.5}Bi_{0.5}O)$CuS and $(La_{0.5}Bi_{0.5}O)$CuSe exhibit the indirect E_g ($\Gamma \to 0.4\Delta$) of 0.529 and 0.256 eV, respectively. On the other hand, $(La_{0.5}Bi_{0.5}O)$CuTe exhibits the indirect E_g (Z $\to$ 0.4Δ) of 0.094 eV. The Ch substitution also increases the split-off energies at Z and Γ points. In the valence band, O 2p states are located at the deep energy levels, leading to the electron-confinement between the insulating $[LaBiO_2]^{2+}$ layers. This result is crucial for thermoelectricity, where $(La_{0.5}Bi_{0.5}O)$CuTe may provide the largest thermoelectricity by comparing S and $n(E)$, mainly contributed by Te $5p_x/p_y$, Cu $3d_{zx}$, and Cu $3d_{zy}$ states. Alongside being located at the bonding and antibonding level, t_{2g} states are also located at the nonbonding level, leading to the partial hybridization of t_{2g} and Ch p orbitals. The result provides new insights and finding, which open experimental works.

Conflicts of interest

There are no conflicts to declare.

Acknowledgements

References

1 M. H. Elsheikh, D. A. Shnawah, M. F. M. Sabri, S. B. M. Said, M. H. Hassan, M. B. A. Bashir and M. Mohamad, *Renewable Sustainable Energy Rev.*, 2014, **30**, 337–355.

2 C. Forman, I. K. Muritala, R. Pardemann and B. Meyer, *Renewable Sustainable Energy Rev.*, 2016, **57**, 1568–1579.

3 H. Jouhara, N. Khordehgah, S. Almahmoud, B. Delpech, A. Chauhan and S. A. Tassou, *Therm. Sci. Eng. Prog.*, 2018, **6**, 268–289.

4 A. Firth, B. Zhang and A. Yang, *Appl. Energy*, 2019, **235**, 1314–1334.

5 G. A. Slack, in *Solid State Physics*, Elsevier, 1979, vol. 34, pp. 1–71.

6 P. Vaqueiro, G. Guélou, M. Stec, E. Guilmeau and A. V. Powell, *J. Mater. Chem. A*, 2013, **1**, 520–523.

7 M. Cutler and N. F. Mott, *Phys. Rev.*, 1969, **181**, 1336–1340.

8 W. Liu, X. Tan, K. Yin, H. Liu, X. Tang, J. Shi, Q. Zhang and C. Uher, *Phys. Rev. Lett.*, 2012, **108**, 166601.

9 G. J. Snyder and E. S. Toberer, *Nat. Mater.*, 2011, **7**, 105–114.

10 R. Venkatasubramanian, E. Siivola, T. Colpitts and B. O'Quinn, *Nature*, 2001, **413**, 597–602.

11 G. Bulman, P. Barletta, J. Lewis, N. Baldasaro, M. Manno, A. Bar-Cohen and B. Yang, *Nat. Commun.*, 2016, **7**, 10302.

12 C. Wan, R. Tian, M. Kondou, R. Yang, P. Zong and K. Koumoto, *Nat. Commun.*, 2017, **8**, 1024.

13 C. Wan, Y. Wang, N. Wang, W. Norimatsu, M. Kusunoki and K. Koumoto, *J. Electron. Mater.*, 2011, **40**, 1271–1280.

14 S. D. Luu and P. Vaqueiro, *Semicond. Sci. Technol.*, 2014, **29**, 064002.

15 Y. Liu, L.-D. Zhao, Y. Liu, J. Lan, W. Xu, F. Li, B.-P. Zhang, D. Berardan, N. Dragoe and Y.-H. Lin, *J. Am. Chem. Soc.*, 2011, **133**, 20112–20115.

16 H. Hiramatsu, K. Ueda, K. Takafuji, H. Ohta, M. Hirano, T. Kamiya and H. Hosono, *Appl. Phys. A*, 2004, **79**, 1521–1523.

17 Y. Zhou and L. D. Zhao, *Adv. Mater.*, 2017, **29**, 1702676.

18 M. Palazzi, C. Carcaly and J. Flahaut, *J. Solid State Chem.*, 1980, **35**, 150–155.

19 M. Palazzi and S. Jaulmes, *Acta Crystallogr., Sect. B: Struct. Crystallogr. Cryst. Chem.*, 1981, **37**, 1337–1339.

20 K. Ueda, S. Inoue, S. Hirose, H. Kawazoe and H. Hosono, *Appl. Phys. Lett.*, 2000, **77**, 2701–2703.

21 S.-i. Inoue, K. Ueda, H. Hosono and N. Hamada, *Phys. Rev. B: Condens. Matter Mater. Phys.*, 2001, **64**, 245211.

22 K. Ueda, S. Inoue, H. Hosono, N. Sarukura and M. Hirano, *Appl. Phys. Lett.*, 2001, **78**, 2333–2335.

23 K. Ueda and H. Hosono, *J. Appl. Phys.*, 2002, **91**, 4768–4770.

24 Y. Ohki, K. Takase, Y. Takahashi, Y. Takano and K. Sekizawa, *J. Alloys Compd.*, 2006, **408–412**, 98–100.

25 Y. Ohki, S. Komatsuzaki, Y. Takahashi, K. Takase, Y. Takano and K. Sekizawa, *AIP Conf. Proc.*, 2006, **850**, 1309–1310.

26 Y. Takano, C. Ogawa, Y. Miyahara, H. Ozaki and K. Sekizawa, *J. Alloys Compd.*, 1997, **249**, 221–223.

27 S. Muhammady, I. M. Sutjahja, A. Rusydi, T. Winata, K. Takase and Y. Darma, *Jpn. J. Appl. Phys.*, 2017, **56**, 121201.

28 F. Li, T.-R. Wei, F. Kang and J.-F. Li, *J. Mater. Chem. A*, 2013, **1**, 11942–11949.

29 L. D. Zhao, D. Berardan, Y. L. Pei, C. Byl, L. Pinsard-Gaudart and N. Dragoe, *Appl. Phys. Lett.*, 2010, **97**, 092118.

30 X. Zhang, C. Chang, Y. Zhou and L.-D. Zhao, *Materials*, 2017, **10**, 198.

31 Y.-L. Pei, H. Wu, D. Wu, F. Zheng and J. He, *J. Am. Chem. Soc.*, 2014, **136**, 13902–13908.

32 Y. Liu, J. Ding, B. Xu, J. Lan, Y. Zheng, B. Zhan, B. Zhang, Y. Lin and C. Nan, *Appl. Phys. Lett.*, 2015, **106**, 233903.

33 D. S. Pankratova, A. P. Novitskii, K. V. Kuskov, I. A. Sergienko, D. V. Leybo, A. T. Burkov, P. P. Konstantinov and V. V. Khovaylo, *Semiconductors*, 2019, **53**, 624–627.

34 H. Wang, S. Li, Y. Liu, J. Ding, Y.-H. Lin, H. Xu, B. Xu and C.-W. Nan, *Sci. Rep.*, 2016, **6**, 24620.

35 H.-C. Chang, H.-J. You, R. Sankar, Y.-J. Yang, L.-C. Chen and K.-H. Chen, *Ceram. Int.*, 2019, **45**, 9254–9259.

36 P. Giannozzi, S. Baroni, N. Bonini, M. Calandra, R. Car, C. Cavazzoni, D. Ceresoli, G. L. Chiarotti, M. Cococcioni, I. Dabo, A. D. Corso, S. d. Gironcoli, S. Fabris, G. Fratesi, R. Gebauer, U. Gerstmann, C. Gougoussis, A. Kokalj, M. Lazzeri, L. Martin-Samos, N. Marzari, F. Mauri, R. Mazzarello, S. Paolini, A. Pasquarello, L. Paulatto, C. Sbraccia, S. Scandolo, G. Sclauzero, A. P. Seitsonen, A. Smogunov, P. Umari and R. M. Wentzcovitch, *J. Phys.: Condens. Matter*, 2009, **21**, 395502.

37 P. Giannozzi, O. Andreussi, T. Brumme, O. Bunau, M. B. Nardelli, M. Calandra, R. Car, C. Cavazzoni, D. Ceresoli and M. Cococcioni, *J. Phys.: Condens. Matter*, 2017, **29**, 465901.

38 H. Hiramatsu, H. Yanagi, T. Kamiya, K. Ueda, M. Hirano and H. Hosono, *Chem. Mater.*, 2008, **20**, 326–334.

39 J. P. Perdew, K. Burke and M. Ernzerhof, *Phys. Rev. Lett.*, 1996, **77**, 3865–3868.

40 S. Muhammady, Y. Kurniawan, M. A. K. Purbayanto and Y. Darma, *Mater. Res. Express*, 2018, **5**, 066303.

41 S. Muhammady, E. Nurfani, R. Kurniawan, I. M. Sutjahja, T. Winata and Y. Darma, *Mater. Res. Express*, 2017, **4**, 024002.

42 N. Troullier and J. L. Martins, *Solid State Commun.*, 1990, **74**, 613–616.

43 N. Troullier and J. L. Martins, *Phys. Rev. B: Condens. Matter Mater. Phys.*, 1991, **43**, 1993–2006.

44 N. Troullier and J. L. Martins, *Phys. Rev. B: Condens. Matter Mater. Phys.*, 1991, **43**, 8861–8869.

45 S. Goedecker, M. Teter and J. Hutter, *Phys. Rev. B: Condens. Matter Mater. Phys.*, 1996, **54**, 1703–1710.

46 C. Hartwigsen, S. Goedecker and J. Hutter, *Phys. Rev. B: Condens. Matter Mater. Phys.*, 1998, **58**, 3641–3662.

47 S. Muhammady, A. S. Erlyanti, R. Widita and Y. Darma, *Int. J. Quantum Chem.*, 2020, **120**, e26090.

48 C. G. Broyden, *IMA J. Appl. Math.*, 1970, **6**, 76–90.

49 R. Fletcher, *Comput. J.*, 1970, **13**, 317–322.

50 D. Goldfarb, *Math. Comput.*, 1970, **24**, 23–26.

51 D. F. Shanno, *Math. Comput.*, 1970, **24**, 647–656.

52 J. D. Head and M. C. Zerner, *Chem. Phys. Lett.*, 1985, **122**, 264–270.

53 Y. Jiang-Ni, Z. Zhi-Yong, Y. Jun-Feng and D. Zhou-Hu, *Chin. Phys. B*, 2010, **19**, 017101.

54 C. J. Fennie and K. M. Rabe, *Phys. Rev. B: Condens. Matter Mater. Phys.*, 2003, **68**, 184111.

55 G. Wu, S. K. Zheng, P. Wu, J. Su and L. Liu, *Solid State Commun.*, 2013, **163**, 7–10.

56 R. Chowdhury, S. Adhikari and P. Rees, *Phys. B: Condens. Matter*, 2010, **405**, 4763–4767.

57 C. G. Broyden, *Math. Comput.*, 1965, **19**, 577–593.

58 K. Momma and F. Izumi, *J. Appl. Crystallogr.*, 2011, **44**, 1272–1276.

59 R. D. Shannon, *Acta Crystallogr., Sect. A: Cryst. Phys., Diffr., Theor. Gen. Crystallogr.*, 1976, **32**, 751–767.

60 M. E. Fleet, *Mineral. Mag.*, 1976, **40**, 531–533.

61 R. Freitag and J. Conradie, *J. Chem. Educ.*, 2013, **90**, 1692–1696.

62 W. E. Brittin, *J. Chem. Educ.*, 1945, **22**, 145.

63 R. G. Pearson, *J. Mol. Struct.: THEOCHEM*, 1983, **103**, 25–34.

64 S. Muhammady, Y. Kurniawan, S. Ishiwata, A. Rousuli, T. Nagasaki, S. Nakamura, H. Sato, A. Higashiya, A. Yamasaki, Y. Hara, A. Rusydi, K. Takase and Y. Darma, *Inorg. Chem.*, 2018, **57**, 10214–10223.

65 D. Zou, S. Xie, Y. Liu, J. Lin and J. Li, *J. Mater. Chem. A*, 2013, **1**, 8888–8896.

66 B. Feng, G. Li, Y. Hou, C. Zhang, C. Jiang, J. Hu, Q. Xiang, Y. Li, Z. He and X. a. Fan, *J. Alloys Compd.*, 2017, **712**, 386–393.

67 J. P. Perdew, *Int. J. Quantum Chem.*, 1985, **28**, 497–523.

68 H.-Y. Lee and J. Robertson, *J. Appl. Phys.*, 2013, **113**, 213706.

69 T. L. Brown, H. E. LeMay, B. E. Bursten and L. S. Brunauer, *Chemistry: The Central Science*, Prentice Hall Englewood Cliffs, New Jersey, 1994.

70 Y. Zhang, X. Yuan, X. Sun, B.-C. Shih, P. Zhang and W. Zhang, *Phys. Rev. B: Condens. Matter Mater. Phys.*, 2011, **84**, 075127.

71 J. Heyd, G. E. Scuseria and M. Ernzerhof, *J. Chem. Phys.*, 2003, **118**, 8207–8215.

72 J. Heyd, G. E. Scuseria and M. Ernzerhof, *J. Chem. Phys.*, 2006, **124**, 219906.

73 J. Paier, M. Marsman, K. Hummer, G. Kresse, I. C. Gerber and J. G. Ángyán, *J. Chem. Phys.*, 2006, **124**, 154709.

74 J. Paier, M. Marsman, K. Hummer, G. Kresse, I. C. Gerber and J. G. Ángyán, *J. Chem. Phys.*, 2006, **125**, 249901.

75 J. Paier, M. Marsman and G. Kresse, *J. Chem. Phys.*, 2007, **127**, 024103.

76 L. Hedin, *Phys. Rev.*, 1965, **139**, A796–A823.

77 W.-D. Schöne and A. G. Eguiluz, *Phys. Rev. Lett.*, 1998, **81**, 1662–1665.

78 J. L. F. Da Silva, M. V. Ganduglia-Pirovano, J. Sauer, V. Bayer and G. Kresse, *Phys. Rev. B: Condens. Matter Mater. Phys.*, 2007, **75**, 045121.

79 S. Das, G. Shi, N. Sanders and E. Kioupakis, *Chem. Mater.*, 2018, **30**, 7124–7129.

80 M. Marsman, J. Paier, A. Stroppa and G. Kresse, *J. Phys.: Condens. Matter*, 2008, **20**, 064201.

81 J. Stewart, *Calculus*, Thomson Brooke/Cole, Ontario, 6 edn, 2009.

82 P. Oelhafen, E. Hauser, H.-J. Güntherodt and K. H. Bennemann, *Phys. Rev. Lett.*, 1979, **43**, 1134–1137.

83 H. M. Meyer III, D. M. Hill, J. H. Weaver, D. L. Nelson and C. F. Gallo, *Phys. Rev. B: Condens. Matter Mater. Phys.*, 1988, **38**, 7144–7147.

84 K. Pal, S. Anand and U. V. Waghmare, *J. Mater. Chem. C*, 2015, **3**, 12130–12139.